Effects of seasonality, transport pathway, and spatial structure on greenhouse gas fluxes in a restored wetland

Gavin McNicol

Cove S. Sturtevant

Sara H. Knox

Iryna Dronova

Dennis D. Baldocchi

Whendee L. Silver
First published: 26 November 2016
https://doi.org/10.1111/gcb.13580
Cited by: 5
UC-eLinks

Abstract

Wetlands can influence global climate via greenhouse gas (GHG) exchange of carbon dioxide (CO_2), methane (CH_4), and nitrous oxide (N_2O). Few studies have quantified the full GHG budget of wetlands due to the high spatial and temporal variability of fluxes. We report annual open-water diffusion and ebullition fluxes of CO_2, CH_4, and N_2O from a restored emergent marsh ecosystem. We combined these data with concurrent eddy-covariance measurements of whole-ecosystem CO_2 and CH_4 exchange to estimate GHG fluxes and associated radiative forcing effects for the whole wetland, and separately for open-water and vegetated cover types. Annual open-water CO_2, CH_4, and N_2O emissions were 915 ± 95 g C-CO_2 m^{-2} yr^{-1}, 2.9 ± 0.5 g C-CH_4 m^{-2} yr^{-1}, and 62 ± 17 mg N-N_2O m^{-2} yr^{-1}, respectively. Diffusion dominated open-water GHG transport, accounting for >99% of $CO_2$and N_2O emissions, and ~71% of CH_4 emissions. Seasonality was minor for CO_2 emissions, whereas CH_4 and N_2O fluxes displayed strong and asynchronous seasonal dynamics. Notably, the overall radiative forcing of open-water fluxes (3.5 ± 0.3 kg CO_2-eq m^{-2} yr^{-1}) exceeded that of vegetated zones (1.4 ± 0.4 kg CO_2-eq m^{-2} yr^{-1}) due to high ecosystem respiration. After scaling results to the entire wetland using object-based cover classification of remote sensing imagery, net uptake of CO_2 (−1.4 ± 0.6 kt CO_2-eq yr^{-1}) did not offset CH_4 emission (3.7 ± 0.03 kt CO_2-eq yr^{-1}), producing an overall positive radiative forcing effect of 2.4 ± 0.3 kt CO_2-eq yr^{-1}. These results demonstrate clear effects of seasonality, spatial structure, and transport pathway on the magnitude and composition of wetland GHG emissions, and the efficacy of multiscale flux measurement to overcome challenges of wetland heterogeneity.

Introduction

Wetlands cover only 5–8% of the Earth's land surface (Mitsch & Gosselink, 2015), but their greenhouse gas (GHG) emissions disproportionately influence global atmospheric radiative forcing (Peters & Conrad, 1996; Falkowski *et al*., 2008; IPCC, 2013). The poor solubility and slow diffusivity of oxygen (O_2) in flooded wetland soil act as a physical constraint to aerobic metabolism, lowering reduction–oxidation (redox) potential, and selecting for biology that can overcome or exploit the anaerobic soil environment (Takai & Kamura, 1966). Structural adaptations of emergent wetland plants, such as porous aerenchyma, facilitate aerobic plant metabolism (Vartapetian & Jackson, 1996), often supporting high primary production under favorable nutrient regimes. In contrast, organic matter decomposition is slower in anaerobic wetland soils (Freeman *et al*., 2001; Megonigal *et al*., 2004) and is therefore typically outpaced by plant biomass production (Bridgham *et al*., 2006), removing carbon dioxide (CO_2) from the atmosphere and leading to the accumulation of large, redox-protected, organic carbon (C) stocks (Limpens *et al*., 2008). However, anaerobic metabolism in wetlands also produces the GHGs methane (CH_4) and nitrous oxide (N_2O), which have considerably stronger instantaneous climate forcing effects than CO_2 (IPCC, 2013). Low redox conditions in wetlands are currently responsible for over one-third of global CH_4 emissions (Bridgham *et al*., 2013). Furthermore, wetland CH_4 emissions increase nonlinearly with temperature (Yvon-Durocher *et al*., 2014), which may lead to a positive feedback to climate change. Wetlands are also increasingly important for retention and filtering of excess reactive nitrogen that drains from surrounding upland soils (Seitzinger *et al*., 2006; Cui *et al*., 2013) and can produce N_2O as an intermediate of O_2-sensitive nitrification and denitrification processes (Firestone & Davidson, 1989; Jungkunst & Fiedler, 2007; Burgin & Groffman, 2012).

The large soil C stock in wetlands, and many ecological cobenefits, has driven global interest and effort in wetland restoration (Zedler & Kercher, 2005; Moreno-Mateos *et al*., 2012), and significant potential for CO_2 sequestration has led to efforts to quantify and predict wetland GHG exchange comprehensively (Bridgham *et al*., 2013; Neubauer & Megonigal, 2015). Early wetland GHG research focused on CH_4 and CO_2 exchange (Matthews & Fung, 1987; Whiting & Chanton, 1993; Whalen, 2005; Bridgham *et al*., 2013), with a more recent focus on quantifying climate change mitigation potential for C stabilization and sequestration (Bridgham *et al*., 2006; Hatala *et al*., 2012a; Knox *et al*., 2015), particularly in restored wetlands (Moreno-Mateos *et al*., 2012). Fluxes of N_2O are less frequently measured, but may be important to measure for at least two reasons. First, N_2O is a very potent GHG, so even relatively low emissions can be important in the overall GHG balance (Neubauer & Megonigal, 2015). Second, N_2O fluxes are highly sensitive to redox conditions, particularly O_2 availability (Venkiteswaran *et al*., 2014; Beaulieu *et al*., 2015; Helton *et al*., 2015), and thus, slight changes

in wetland biogeochemistry could affect fluxes of N_2O (Moseman-Valtierra, 2012; Weston *et al.*, 2014). Improved observation of spatial and temporal dynamics in O_2- or redox-sensitive gas fluxes such as $CH_4$and N_2O is also needed to advance our overall understanding of heterotrophic metabolism in low and variable redox ecosystems (Silver *et al.*, 1999; Pett-Ridge & Firestone, 2005; Hall *et al.*, 2012; Davidson *et al.*, 2014), and to test biophysical models of ecosystem CO_2, CH_4, and N_2O dynamics (Davidson & Janssens, 2006; Von Fischer & Hedin, 2007; Davidson *et al.*, 2012; McNicol & Silver, 2014; Oikawa *et al.*, 2014). Simultaneous measurement of GHG fluxes is therefore important to quantify wetland GHG budgets, but may also improve our understanding of low redox ecology.

Wetlands often exhibit high spatial heterogeneity in vegetation and hydrology that present challenges to estimating GHG exchange (Bridgham *et al.*, 2013). Multiple transport pathways are sensitive to biophysical forcings at different timescales, and thus produce nonlinear and asynchronous gas flux dynamics at the ecosystem scale (Sturtevant *et al.*, 2016). Emissions pathways include plant-mediated flow and sediment ebullition (bubbling events) that facilitates gas-phase transport, and diffusive fluxes at the air–water interface that emits dissolved-phase gases. Emergent plants are thought to be important in wetland GHG exchange (Laanbroek, 2010) due to their high productivity, respiration, and aerenchyma transport of sediment CH_4 (Armstrong *et al.*, 1991). However, data on other modes of GHG emission are scarce (Bridgham *et al.*, 2013). Estimates of ebullitive GHG fluxes in particular require high spatial and temporal replication because ebullition is a stochastic process that is both spatially heterogeneous and episodic (Wik *et al.*, 2016). Physical triggers of ebullition such as changes in barometric pressure and water depth (Wik *et al.*, 2013) are superimposed on rates of bubble formation and growth (Scandella *et al.*, 2011), which occurs when production of poorly soluble CH_4 pushes local gas partial pressures above the local hydrostatic pressure (Chanton *et al.*, 1989; Scandella *et al.*, 2011; Green, 2013). Other bubble gases include CO_2, N_2, and O_2 that diffuse into the gas phase according to their local partial pressure and gas concentrations in bubbles vary widely between and within ecosystems over time (Tokida *et al.*, 2012; Martinez & Anderson, 2013; Wik *et al.*, 2013; Crawford *et al.*, 2014; Hamilton *et al.*, 2014). We know of no studies that have considered fluxes of N_2O via ebullition. Diffusion across the air–water interface is an additional pathway for wetland GHG emissions. Fluxes are driven by the concentration gradient and turbulent mixing of adjacent fluids (Kling *et al.*, 1992; Cole & Caraco, 1998) producing controls at several timescales: second-to-minute variation in wind speed (Matthews *et al.*, 2003); diel cycles of thermal stratification and convective mixing in the water column (Poindexter & Variano, 2013; Koebsch *et al.*, 2015); and the diel to seasonal cycles of biogenic GHG production.

Pairing of gas flux measurements made at different scales or that capture different transport pathways may help overcome the challenge of wetland heterogeneity. Tower-based approaches such as eddy covariance provide quasi-continuous measurement of gas exchange at the ecosystem scale and can greatly improve our ability to quantify fluxes of GHG (Baldocchi *et al*., 1988; Baldocchi, 2003). Eddy-covariance observations have helped separate the effects of temperature and gross primary production (GPP) on rice paddy CH_4 fluxes (Knox *et al*., 2016) and can be used to parse out sources of spatial (Matthes *et al*., 2014) and temporal (Hatala *et al*., 2012b; Koebsch *et al*., 2015; Sturtevant *et al*., 2016) variability in wetland CH_4fluxes. Furthermore, these approaches can be coupled to spatially explicit GHG flux measurements using chambers that are useful for identifying hot spots at the ecosystem scale (Teh *et al*., 2011). Emergent wetlands in particular may benefit from this coupled approach as dense plant canopies necessitate tower-based flux measurement while manual-sampling approaches can be used to distinguish patterns in open-water gas flux via ebullition and diffusion.

In the present study, we draw on the advantages of both eddy covariance and highly replicated and long-term manual-sampling approaches to quantify annual wetland exchange of CO_2, CH_4, and N_2O. We used these data to understand how GHG fluxes and their radiative forcing effects vary with ecosystem seasonality, transport pathway of emission, and spatial structure.

Materials and methods

Site description

The study was conducted at Mayberry Farms (38.0498°N 121.7651°W), an Ameriflux site (US-Myb), located in the western portion of the Sacramento Delta, California (Fig. 1a). The western Delta experiences a Mediterranean climate with a 30-year mean air temperature of 16.4 °C and an annual precipitation rate of 336 mm (1981–2010, Antioch, CA, USA). Winters are cool and wet, and summers are hot and dry, with mean monthly temperatures ranging from 7.9 °C in January to 24.1 °C in July. Much of the former wetlands of the Delta were reclaimed for drained agriculture during the last century, leading to rapid peat soil oxidation (Drexler *et al*., 2009a). Mayberry Farms was restored from a drained agricultural peatland to a wetland in October 2010 (Knox *et al*., 2015). The wetland is a large (1.21 km^2) emergent freshwater marsh with a continuous hydro-period maintained by managed inflow of adjacent river water during the dry summer months, and rainfall during winter, to compensate for evaporative losses. There is no outflow of water from the wetland, but prevailing westerly winds structure hydrologic flow from approximately NW to SE within wetland tracts that are separated by berms. The restored wetland

exhibited a mosaic pattern of open-water pools (1–2 m deep) and dense vegetation patches of emergent macrophytes *Schoenoplectus* spp. and *Typha* spp. in shallower areas. The submerged bathymetry-associated aboveground cover-type mosaic was an intentional part of the design and construction of the wetland, while the vegetation regenerated naturally (Knox *et al*., 2015). Underlying soils are deep (>5 m) and peaty (Typic Haplosaprists), but surface layers are heavily subsided (Drexler *et al*., 2009b) exhibiting ~20% C, neutral pH, and large redox-active iron (Fe) pool (McNicol & Silver, 2014).

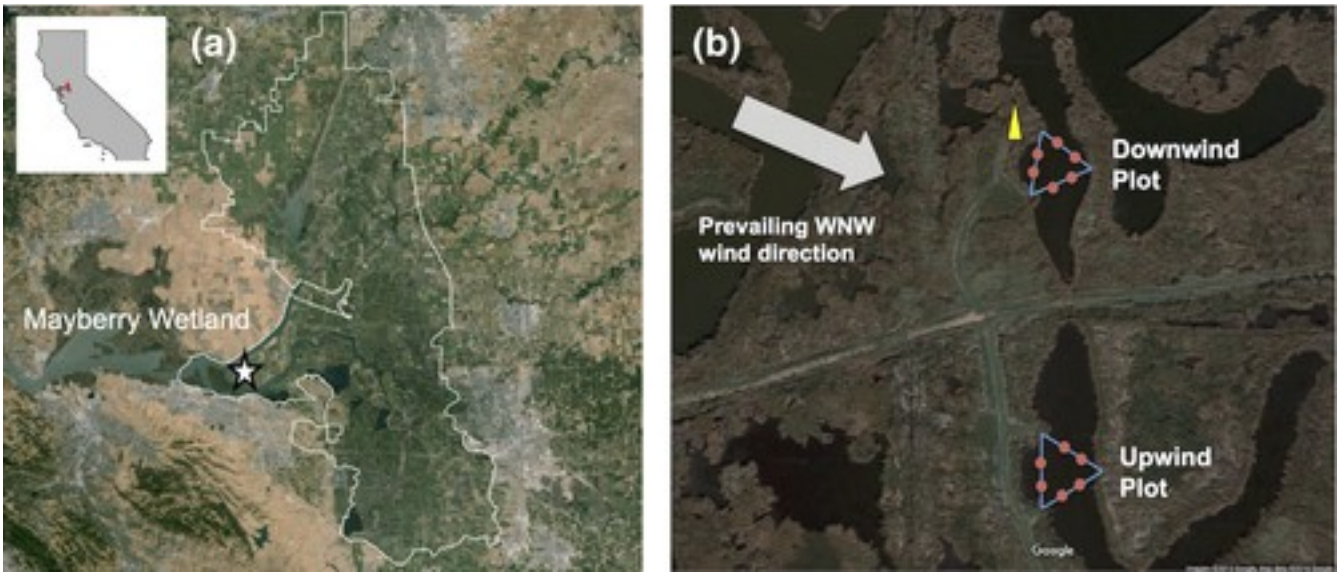

Figure 1
Open in figure viewerPowerPoint
(a) Regional map showing position of Mayberry Farms within the Sacramento Delta, California, and (b) Google Earth image of site showing position of the downwind and upwind plots (large triangles), approximate ebullition chamber locations within plots (circles), eddy-covariance flux tower (filled triangle), and prevailing WNW wind direction (white arrow). [Colour figure can be viewed at wileyonlinelibrary.com].
Caption

Study design

We measured wetland CO_2, CH_4, and N_2O emissions via ebullition and diffusion, and whole-ecosystem CO_2 and CH_4 emissions, for 1 year (February 20, 2014, to February 20, 2015) to estimate total GHG fluxes, explore effects of seasonality, and compare GHG fluxes between wetland plots (upwind and downwind) and cover-type zones (open-water and vegetated). Manual sample collection for ebullition and diffusive fluxes was approximately weekly (49 sampling dates), while whole-ecosystem exchange was measured continuously from an eddy-covariance flux tower (Fig. 1b). We stratified our manual sampling with plots at hydrologic end-members upwind and downwind of open-water tracks exposed to the prevailing WNW winds, both within

300 m of the eddy-covariance tower. At both plots, we inserted three T-posts into shallow vegetated soil at the edges of pools to form the vertices of a triangle. Ropes were suspended between these posts to allow for low disturbance sample collection from a lightweight inflatable boat (Fig. 1b).

Ebullitive and diffusive fluxes

Continuous records of ebullition gas release were collected (n = 6, per plot) using permanently deployed chambers that were adapted from Varadharajan *et al*. (2010). Briefly, an inverted 45.7-cm-diameter polyethylene funnel (United States Plastics Corp®, Lima, OH, USA) collected bubbles released from a 0.17-m^2 sediment footprint and transferred gas up into a transparent 5 × 60 cm PVC tube. The ~1-m-tall chamber design allowed full submergence in the shallow water column of the wetland, while being suspended 10–20 cm from a buoy at the water surface to avoid disturbing the sediment. Approximately weekly, a 30-ml syringe was used to quantitatively sample chamber gas via a ¼″ stainless-steel union tee at the top of the collection tube. Collection time and sample volume was recorded for each chamber, and the transparent collection tube was checked after sampling to ensure complete gas collection. We overpressurized 30 ml subsamples of gas for subsequent analyses in pre-evacuated 20-ml serum vials crimped with butyl rubber stoppers (Geo-Microbial Technologies, Ochelata, OK, USA). Occasional maintenance was also required on the chambers including replacing sampling port septa, cleaning the interior of the sampling chamber, and fixing leaks, which produced some data gaps in the ebullition record. Resulting data gaps represented 2–20% of the individual chamber time series and were filled using the overall median flux rate from the respective chamber. The weekly sampling of permanent chambers may lead to randomly distributed underestimations of CO_2, CH_4, and N_2O bubble concentrations due to back-diffusion into the water column (Varadharajan *et al*., 2010; Wik *et al*., 2013). However, permanent chambers were selected to meet the need for highly replicated and long-term measurements campaigns to estimate ebullition fluxes (Wik *et al*., 2016), while the sensitivity of final GHG emission estimates to bubble GHG content is more readily evaluated *post hoc*.

Dissolved GHG concentrations used to calculate diffusive fluxes were measured in triplicate at each plot, with one sample from the midway point of each rope (Fig. 1b). Water was collected at 10 cm below the surface in a pre-evacuated 60-ml vial that had been backfilled with 10 ml ultrahigh purity N_2 (99.999%; Praxair Inc., Richmond, CA, USA) to provide a sampling headspace. Microbial activity that might affect dissolved gas content, such as aerobic CH_4oxidation, was eliminated by preweighing KCl salt into the vials (~3.7 g) to achieve a final concentration of at least 2 M KCl after sample collection (Matthews *et al*., 2003).

Gas concentration analyses were typically conducted within 6–12 h of collection and always within 24 h. Both sets of gas samples were analyzed on a Shimadzu GC-14A (Shimadzu Scientific Inc., Columbia, MD, USA) for CO_2, CH_4, and N_2O concentrations using thermal conductivity, flame ionization, and electron capture detectors, respectively. The GC was calibrated with standard gas containing 997 ppm(v) CO_2, 9.91 ppm(v) CH_4, and 10.4 ppm(v) N_2O (Praxair Inc., Los Angeles, CA, USA) which were run every 10 samples. As many ebullition gas samples contained percent-range CH_4 concentrations, we reduced detector sensitivity and ran a high-CH_4 standard (99.0%; Restek®, Bellefonte, PA, USA) to permit linear extrapolation from one-point calibration. Run precision on standards (C.V.) was always <2%. Water samples were equilibrated to room temperature (~24 °C) then vigorously shaken by hand for 2 min, and left to settle for a further 2 min, before the equilibrated headspace was sampled for GC analysis.

Ebullition gas fluxes were calculated from the product of the weekly bubble flux and bubble CO_2, CH_4, and N_2O mole fractions, and were normalized by the cross-sectional area of the ebullition chamber. Diffusive fluxes were estimated with Fick's law:

$$F = k\left([\mathrm{GHG}]_{\mathrm{sfc}} - [\mathrm{GHG}]_{\mathrm{eq}}\right), \quad (1)$$

$[GHG]_{sfc}$ and $[GHG]_{eq}$ are observed and equilibrium dissolved concentrations, respectively, of CO_2, CH_4, or N_2O, and k (m day^{-1}) is the gas transfer coefficient. Equilibrium dissolved GHG concentrations were calculated using Henry's law and assumed ambient GHG concentrations of 400 ppm(v) CO_2, 2 ppm(v) CH_4, and 450 ppb(v) N_2O. Henry's law constants (H) are temperature dependent according to Sander (2015):

$$H(T) = H\theta \times \exp\left(\frac{-\Delta_{sol}H}{R}\left(\frac{1}{T} - \frac{1}{T\theta}\right)\right), \quad (2)$$

where $H\theta$ is the Henry's law constant at a reference temperature ($T\theta$ = 298.15 K), T is measured *in situ* or sample water temperature, and $-\Delta_{sol}H/R$ is a constant describing the enthalpy of solution. Constants used in these calculations are tabulated in Sander (2015).

We estimated the gas transfer coefficient, k, using a literature parameterization with U_{10} (Cole & Caraco, 1998):

$$k_{600}(\mathrm{m\ d^{-1}}) = 2.07 + 0.215U_{10}^{1.7}, \quad (3)$$

U_{10} is horizontal wind speed measured extrapolated to 10 m using the theoretical log wind profile equation:

$$\frac{U_{10}}{U_z} = \frac{\ln\left(\frac{10-d}{z_0} + \psi_{U10}\right)}{\ln\left(\frac{z-d}{z_0} + \psi_{U10}\right)}, \quad (4)$$

where U_z is the observed horizontal wind speed at height z, d is the zero plane displacement of the canopy (m), and z_0 is the roughness length of the canopy (m). The term ψ_{U10} depends on atmospheric stability. Under stable conditions ($z/L > 0$), ψ_{U10} is computed according to:

$$\psi_{U10}\left(\frac{z}{L}\right) = \frac{4.7z}{L}, \quad (5)$$

And under unstable conditions ($z/L < 0$) according to:

$$\psi_{U10}\left(\frac{z}{L}\right) = -2\ln\left[\frac{(1+x)}{2}\right] - \ln\left[\frac{(1+x^2)}{2}\right] + 2\tan^{-1}(x) - \frac{\pi}{2}, \quad (6)$$

where L is the Obukhov length calculated half-hourly from micrometeorological data, and $x = [1 - (15z/L)]^{1/4}$ (Stull, 2012).

Study period k_{600} values were then computed from Eqn 3 and U_{10}, and adjusted to gas-specific k values for CO_2, CH_4, and N_2O using relevant Schmidt numbers (Wanninkhof, 1992) and the following relationship (Jähne *et al.*, 1987):

$$\frac{k_{gas1}}{k_{gas2}} = \left(\frac{Sc_{gas1}}{Sc_{gas2}}\right)^n, \quad (7)$$

where Sc is the temperature-dependent Schmidt number of the respective gas and the exponent, n, varies from 0.5 to 0.67 and describes the turbulence conditions at the aqueous surface. We selected a value of 0.5 suitable for more turbulent conditions and higher wind speeds (Jähne *et al.*, 1987) although k and resulting flux estimates were insensitive to changing n to 0.67, and the range of k did not change considerably when separately estimated using u^* rather than U_{10} as the explanatory variable.

As with other empirical parameterizations (Wanninkhof, 1992), k_{600} was derived from rates of inert tracer loss (SF_6) over flat fetches of open water across a variety of lake sizes and wind speeds (Cole & Caraco (1998), whereas the presently studied wetland featured canyon-like stretches of connected open-water pools bordered by tall emergent vegetation, which may reduce turbulence close to the air–water boundary. It is also important to consider whether boundary layer assumptions are invalidated before applying parameterizations developed at other sites under different canopy or micrometeorological conditions, and what biases these differences may produce in resulting flux estimates. In this study, diffusive exchange calculations using the k parameterization of Cole & Caraco (1998) likely represent an upper bound for this pathway of GHG emission. A recent study (Cole *et al.*, 2010) found reasonable agreement (within 16%) between performance of empirical wind speed models and manual estimation approaches, though urged independent estimations of k when possible. We were also able to independently evaluate the model's performance by comparing modeled open-water diffusive CO_2 emissions with flux tower emissions during winter when primary production should be negligible. Chemical

enhancement of CO_2 diffusive fluxes was assumed to be negligible due to the neutral pH of wetland water (Emerson, 1975).

Eddy-covariance fluxes

Whole-ecosystem exchange of CO_2 and CH_4 was measured adjacent to the chamber sampling plots using the eddy-covariance technique (Fig. 1), along with supporting environmental measurements as described in Knox *et al.* (2015). A sonic anemometer (Windmaster, Gill Instruments Ltd., Lymington, Hampshire, UK) measured high-frequency three-dimensional wind speed components and virtual temperature at 4.6 m above the water surface. Open-path infrared gas analyzers measured molar concentrations of CO_2, H_2O (LI-7500A; LI-COR Biosciences Inc., Lincoln, NE, USA), and CH_4 (LI-7700; LI-COR Biosciences Inc.). Raw fluxes were recorded at 20-Hz and 30-min fluxes were computed using in-house MATLAB software (Detto *et al.*, 2010; Hatala *et al*., 2012b; Knox *et al*., 2015). Supporting environmental measurements included air temperature and relative humidity (HMP45C; Vaisala, Vantaa, Finland). Soil temperature was recorded at a depth of 8 cm beneath the vegetated soil surface and represented 30-min averages observations from three copper constant thermocouples. Full details on eddy-covariance data collection and processing, and supporting micrometeorological measurements, are described in Knox *et al*. (2015).

Based on quality control procedures described in Knox *et al*. (2015) and periods of power loss and sensor malfunction, the percentage of 30-min fluxes excluded during the study period was 35% for CO_2 fluxes and 32% for CH_4 fluxes. Energy balance closure as calculated in Knox *et al*. (2015), and defined as the energy balance ratio (Wilson *et al*., 2002), was 85% for the study period. Energy balance closure reported in this study falls within the range generally recorded at sites within the FLUXNET network (Wilson *et al*., 2002; Stoy *et al*., 2013). An artificial neural network (ANN) approach was used to gap fill CO_2 and CH_4 fluxes (Baldocchi *et al*., 2015; Knox *et al*., 2015). Carbon dioxide exchange was gap-filled with two separate ANNs, one for daytime conditions and the other for nighttime. Predictions from the ANN resulting from the nighttime gap filling were used to model ecosystem respiration (ER) for both daytime and nighttime periods and ecosystem photosynthesis (GPP) was calculated by subtracting gap-filled CO_2 exchange from modeled respiration (Baldocchi *et al*., 2015). Annual sums of CO_2 and CH_4 exchange were calculated by integrating gap-filled and partitioned fluxes over time, from February 20, 2014, to February 20, 2015. Flux detection limits have been estimated for this system at 0.31 μmol m^{-2} s^{-1} and 3.41 nmol m^{-2} s^{-1} for CO_2 and CH_4, respectively (Detto *et al*., 2011). Error bounds on cumulative eddy-covariance fluxes reflect the 95% confidence interval for the gap-filling procedure (See Knox *et al.*, 2015).

Estimating zone fluxes and radiative forcing

A simple mixing model was used to estimate weekly CO_2 and CH_4 emissions from vegetated wetland areas by combining tower and open-water flux observations:

$$F_{veg} = \frac{(F_{eco} - f_{wat} \times F_{wat})}{f_{veg}} \quad (8)$$

F_{eco} is eddy-covariance net CO_2 (NEE) or CH_4 flux rate, F_{veg} and F_{wat} are CO_2 or CH_4 emissions from vegetation and open-water zones, respectively, and f_{veg} and f_{wat} are the spatial fractions of vegetation and open water within the eddy-covariance flux tower footprint. Open-water zone fluxes (F_{wat}) were calculated as the sum of diffusive and ebullition emissions.

Plane-derived remote sensing imagery and flux footprint modeling were used to estimate the spatial extent and fractions (f_{veg} and f_{wat}) of cover types in the wetland. Vegetated and open-water zones were delineated and their relative spatial extents quantified, using a high-resolution aerial image of the wetland acquired by Eagle Digital Imaging Inc. (Corvallis, OR, USA) in visible and near-infrared spectral regions with ground sampling distance of 0.1524 cm on August 14, 2014. The cover classification therefore captured the state of the wetland midway through the study period, and toward the end of the growing season, during the maximum extent of emergent vegetation. Cover-type delineation was performed using an iterative object-based image analysis (Blaschke, 2010; Dronova, 2015) in eCognition software v.8 (Trimble Inc., Sunnyvale, CA, USA). The image was first segmented into primitive objects using multiresolution segmentation algorithm to generate mapping units representing small patches and patch elements while smoothing local noise (Benz *et al*., 2004). Primitive objects were then classified into vegetation and water using a supervised machine-learning *k*-nearest neighbor classifier. Training samples for vegetation and water were determined using the local maxima of the vegetation index (estimated as normalized difference of near-infrared and red image bands) and water index (normalized difference of green and near-infrared image bands), respectively. Additional object-based rules were further applied to address class confusions at vegetation–water edges and to assign bright ripples caused by wind within the open water extent to the water class. Finally, the classification output was manually revised to correct for the remaining confusion of floating algae, debris, and ripples with emergent vegetation.

The spatial classification of vegetation and open-water zones was combined with an in-house eddy-covariance flux footprint model in R to estimate the fractions of each zone (f_{veg}, f_{wat}) contributing to tower fluxes. Flux footprints were modeled with a semi-analytical model based on Hsieh *et al*. (2000) and extended 2-d by Detto *et al*. (2006). The R packages maptools and sp

were used to assign half-hourly weighted flux footprint pixel locations to either vegetated or open-water portions of the cover classification shapefile (Fig. S1). Periods in which the flux footprint extended beyond the wetland as well as the presence of access berms within flux footprints meant cover types from the two fractions did not always sum to 1. To address this, half-hourly flux periods (16%) below a threshold coverage value of 0.85 were removed; however, approximately 90% of fluxes were consistently captured by the two fractions in the analysis.

The sustained global warming potential (SGWP) of open-water and vegetated zone GHG exchange was calculated using fluxes (g C or N m^{-2} yr^{-1}) converted into kg GHG m^{-2} yr^{-1}, then converted to kg CO_2-eq m^{-2} yr^{-1} using 45 and 270 as respective warming potentials for $CH_4$and N_2O over a 100-year time horizon (Neubauer & Megonigal, 2015). Unlike previous analyses to parse CO_2 emissions using partitioned ER, we calculated SGWP using net ecosystem exchange (NEE), which accounts for uptake and emission of CO_2. We also assumed ecosystem N_2O efflux was comparable to open-water diffusive N_2O fluxes (i.e., no effect of vegetation). Upscaled estimates of flux SGWP were estimated using the respective spatial coverage of vegetation and open water at the site quantified during the cover-type classification. Ecosystem switchover time, defined as the time horizon for the wetland GHG fluxes to change from a net warming effect to a net cooling effect, was estimated using the ratio of CO_2 uptake to CH_4 emissions with the assumption that current flux rates are at steady state (Neubauer, 2014).

Data reporting and statistical analyses

Seasonal averages of gas concentrations and fluxes are reported as medians with 1st to 3rd quartile ($Q_{1–3}$) ranges due to frequency of exponential data distributions. We report dissolved GHG concentrations in ppm(v) in air to permit direct comparison with ebullition gas inventory. Cumulative annual GHG fluxes are reported as the mean ±1 SE, or median and $Q_{1–3}$. Significant ($P < 0.05$) seasonal differences in average gas concentrations and ebullition rates were tested using linear regression analyses in R and concentration data were log-transformed when necessary for the distribution of residuals to meet assumptions of normality.

Results

Ecosystem seasonality

Mean daily soil temperature during the study varied from 20.1 °C in July 2014 to 9.8 °C in January 2015 with an annual average of 16.7 °C (Fig. 2). Peak half-hourly ecosystem GPP preceded peak temperature, ranging from a maximum monthly mean of −20.3 μmol CO_2 m^{-2} s^{-1} in

June 2014 to −0.5 μmol m^{-2} s^{-1} in February 2015. We defined four seasons (spring, summer, fall, and winter) for the wetland ecosystem using trends in temperature and GPP (Fig. 2). Spring (Mar–May) captured the increasing temperatures of the early growing season, summer (June–August) captured annual temperature maxima of the late growing season, fall (September–November) captured the cooling temperatures of early plant senescence, and winter (December–February) captured the annual temperature minima during late plant senescence.

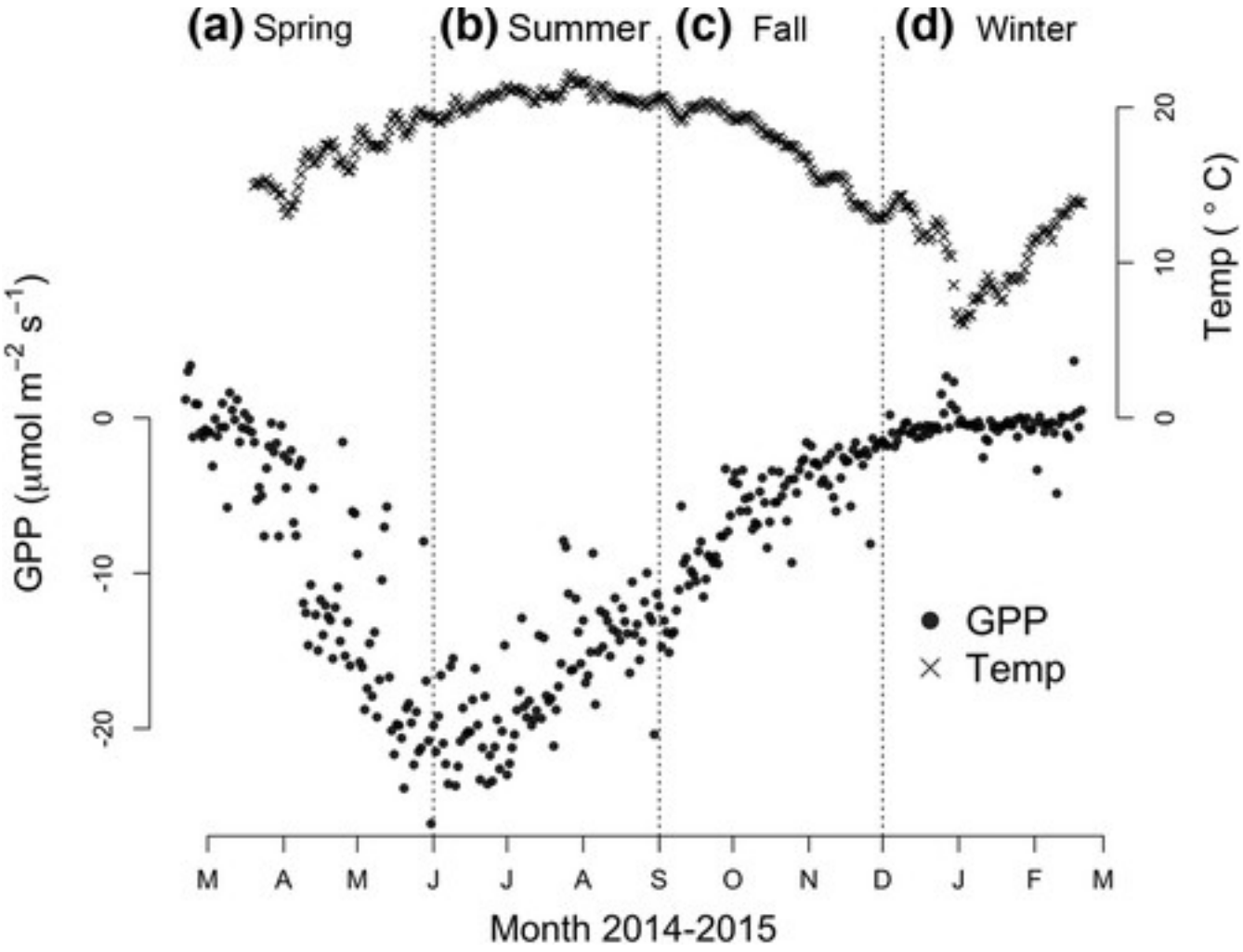

Figure 2

Open in figure viewerPowerPoint

Ecosystem seasonal variation in daily average soil temperature (8 cm) and daily average gross primary productivity (GPP) for Mayberry Farms wetland between March 2014 and 2015. Four distinct seasons (a, b, c, and d) are defined using temp (T) and GPP trends: (a) spring (increasing T, growing season), (b) summer (T_{max}, growing season), (c) fall (decreasing *T*, vegetation senescing), and (d) winter (T_{min}, vegetation senescing).

Caption

Ebullition

We collected a total of 588 ebullition flux observations integrating gas accumulation across approximately 1-week intervals. Ebullition fluxes followed a non-normal exponential distribution (Fig. S2) with many weeks of low fluxes and few weeks of large fluxes. The overall median (Q_1–Q_3) ebullition flux rate was 171 (range: 0–469) ml m^{-2} $week^{-1}$ with a cumulative annual flux of 17.6 (range: 9.97–21.8) l m^{-2} yr^{-1} (Fig. 3). Median rates were significantly higher in the downwind plot, at 250 (range: 65–535) ml m^{-2} $week^{-1}$, than in the upwind plot at 101 (range: 0–403) ml m^{-2} $week^{-1}$, and downwind plot ebullition rates exhibited significant seasonality ($P < 0.1$), ranging between 429 (range: 169–678) ml m^{-2} $week^{-1}$ in summer and 166 (range: 3–364) ml m^{-2} $week^{-1}$ in winter. Despite high week-to-week variability, annual cumulative ebullition fluxes were well approximated by a linear fit (Fig. 3) with a slope of 364 ml m^{-2} $week^{-1}$ ($R^2 = 0.73$) in the downwind plot and 259 ml m^{-2} $week^{-1}$ ($R^2 = 0.55$) in the upwind plot, reflecting greater and more regular ebullition in the downwind plot.

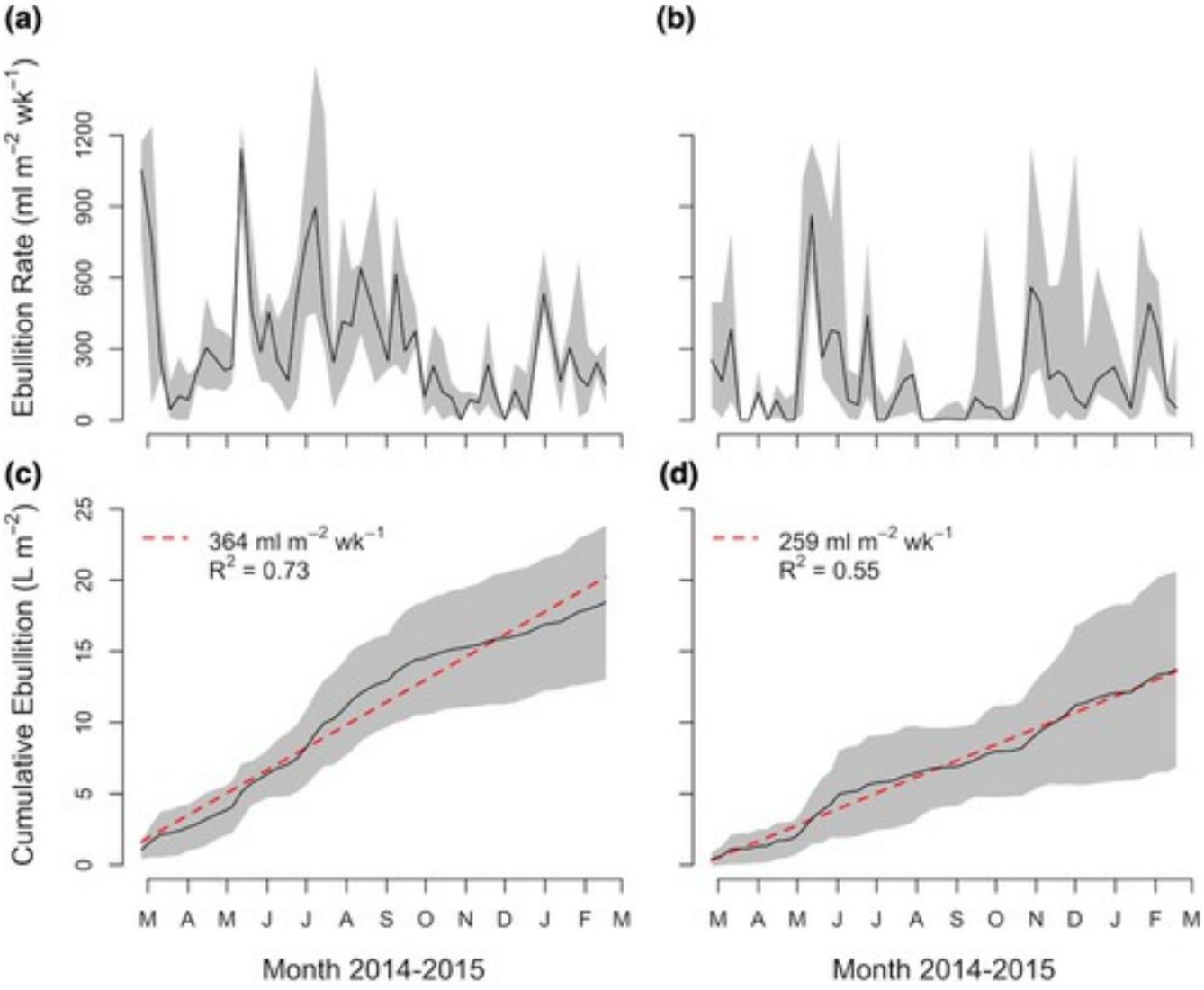

Figure 3
Open in figure viewerPowerPoint
Median weekly ebullition rates (solid line) with interquartile range ($Q_{1–3}$; shaded area) and cumulative fluxes for downwind (a, c) and upwind (b, d) plots. The annual average rate (dashed line) is approximated with a linear fit. [Colour figure can be viewed at wileyonlinelibrary.com]. Caption

Bubble and dissolved GHG content

Weekly bubble GHG content differed due to hydrologic flow (upwind vs. downwind) and seasonality (Table 1; Fig. S3). The annual median bubble CO_2 concentration was 1.03%, was consistently higher in the downwind plot, and ranged seasonally across 1 order of magnitude from a fall maximum of 1.59% in the downwind plot to a spring minimum of 0.38% at the upwind plot. The annual median CH_4 concentration was 0.07%, was also consistently higher in the downwind plot, and ranged seasonally across four orders of magnitude from a summer maximum of 21.08% in the downwind plot, to a winter minimum of 0.01%. The annual median N_2O bubble concentrations was 0.56 ppm(v) and, contrasting with CO_2 and CH_4 content, was consistently lower in the downwind plot. Bubble N_2O ranged seasonally across two orders of magnitude from a summer minimum of 0.08 ppm(v) in the downwind plot to a winter maximum of 3.01 ppm(v) in the upwind plot. Carbon dioxide and CH_4 bubble content always exceeded ambient atmospheric concentrations, whereas N_2O content was close to ambient concentrations in spring, but fell below it in summer, and exceeded it greatly in fall and winter.

Table 1. Median gas (CO_2, CH_4, N_2O) concentrations by inventory (sediment gas vs. dissolved gas), plot (downwind (D) vs. upwind (U)), and season

Inventory	Gas	Plot	Season				Annual
			Spring	Summer	Fall	Winter	
Sed. Gas	[CO_2] (%)	D	1.06[a]	1.03[a]	1.59[b]	0.98[a]	1.03
		U	0.38[a]	0.95[b]	1.38[c]	0.94[b]	
	[CH_4] (%)	D	1.25[a]	21.08[b]	0.05[c]	0.01[d]	0.07

Inventory	Gas	Plot	Season				Annual
			Spring	Summer	Fall	Winter	
Sfc. Gas	$[N_2O]$ (ppm(v))	U	0.02[a]	9.42[b]	0.03[a]	0.01[c]	0.56
		D	0.44[a]	0.08[b]	0.53[a]	1.39[c]	
	$[CO_2]$ (%)	U	0.44[a]	0.28[a]	1.39[b]	3.01[c]	0.40
		D	0.43[a]	0.35[b]	0.36[b]	0.65[c]	
	$[CH_4]$ (ppm(v))	U	0.20[a]	0.26[b]	0.47[c]	0.63[d]	135
		D	361[a]	412[b]	43[c]	114[c]	
	$[N_2O]$ (ppm(v))	U	91[a]	248[b]	96[a]	107[a]	0.46
		D	0.45[a]	0.46[a]	0.41[a]	0.91[b]	
			0.45[a]	0.47[a]	0.37[a]	0.99[b]	

- Superscript characters ($^{a-d}$) denote significant seasonal differences between data distributions for each plot.

Weekly surface (10 cm) dissolved GHG concentrations did not differ significantly with wetland hydrologic flow (between plots) but did show significant seasonal patterns that were similar to ebullition bubble content (Table 1; Fig. S4). The median dissolved CO_2 concentration was 0.40% and had a small seasonal range from a winter maximum of 0.64% to a spring minimum of 0.32%. The median CH_4 concentration was 135 ppm(v) and had a large seasonal range from a summer maximum of 330 ppm(v) to a minimum of 90 ppm(v) during fall and winter. The median dissolved N_2O concentrations was 0.46 ppm(v) and ranged seasonally between a winter maximum of 0.95 ppm(v) and 0.44 ppm(v) during spring, summer, and winter. Similar to bubble content, dissolved CO_2 and CH_4 concentrations always exceeded equilibrium concentrations. However, dissolved N_2O was at equilibrium with the atmosphere during spring and summer, dipped below equilibrium in fall, and then exceeded it during winter.

Ebullition bubble CH_4 and N_2O concentrations were both highly seasonal and asynchronous (Fig. 4). A strong threshold was observed between annual CH_4 and N_2O bubble concentration where high CH_4 (>10%) was observed with low N_2O (<1 ppm(v)), and high N_2O (>1 ppm(v)) was observed with low CH_4 (<0.1%). Moreover, these inverse trends in gas concentration followed a strong seasonal pattern with the highest CH_4:N_2O in summer, and the lowest CH_4:N_2O in winter.

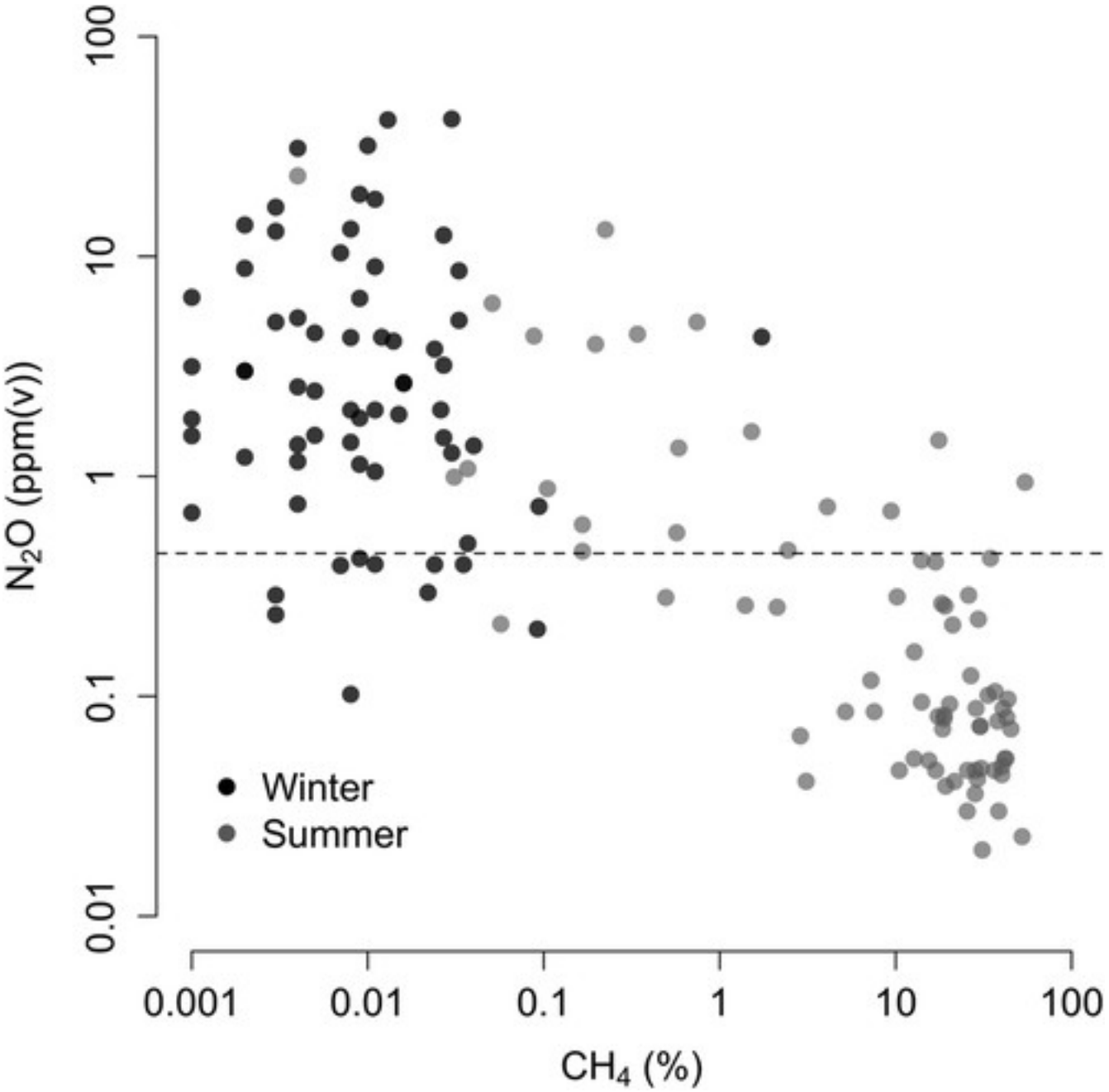

Figure 4

Open in figure viewerPowerPoint

Threshold effect and temporal asynchronicity for CH_4 and N_2O concentrations in ebullition bubbles. Dashed line is N_2O concentration expected at atmospheric equilibrium.

Caption

GHG fluxes

Ebullition GHG flux dynamics (Fig. 5a–c) reflected patterns in bubble gas concentrations. Ebullition CO_2 fluxes were aseasonal and ranged from ~0.1 μmol C-CO_2 m^{-2} s^{-1} in the upwind

plot to ~0.4 μmol C-CO_2 m^{-2} s^{-1} in the downwind plot. Seasonality was stronger in CH_4ebullition with peak emissions of 10–20 nmol C-CH_4 m^{-2} s^{-1} in the downwind plot in summer, contrasting with negligible fall and winter emissions. Conversely, N_2O ebullition was negligible spring to fall, but peaked at ~0.5 pmol N-N_2O m^{-2} s^{-1} in winter.

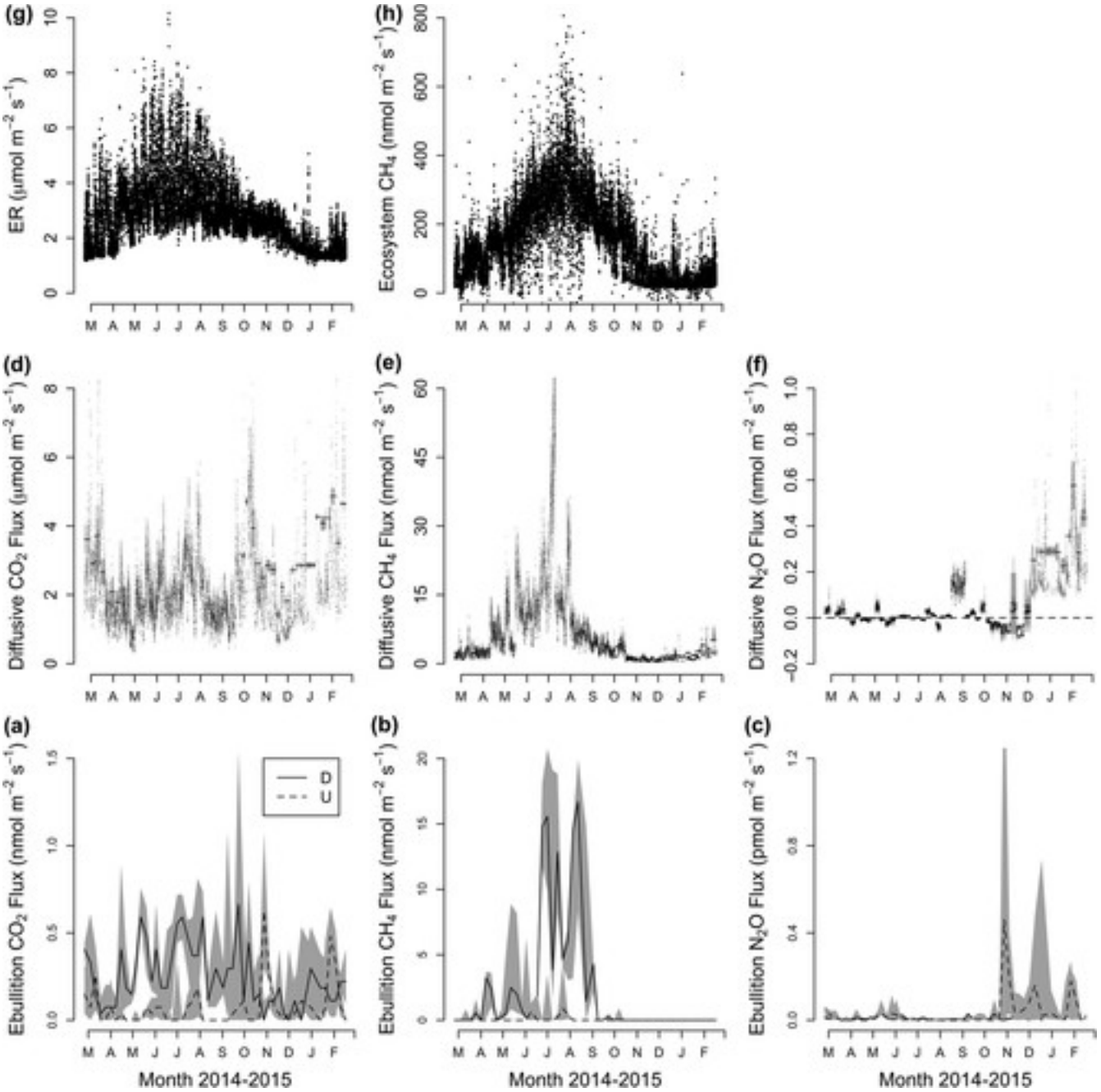

Figure 5

Open in figure viewerPowerPoint

Open-water GHG (CO_2, CH_4, and N_2O) fluxes via ebullition (a–c) and diffusion (d–f), and half-hourly eddy-covariance flux tower observations of ecosystem respiration (ER) and CH_4exchange

(g, h) for the study period March 2014–2015. Ebullition fluxes from downwind (D) and upwind (U) plots are distinguished.

Caption

Diffusive GHG flux dynamics (Fig. 5d–f) displayed short-term (minutes–days) variation driven by wind speed fluctuations superimposed on longer-term seasonality driven by concentration dynamics. Diffusive CO_2 emissions ranged from 0.3 to 11.9 μmol C-CO_2 m^{-2} s^{-1} and were highest on average in winter (2.9 μmol C-CO_2 m^{-2} s^{-1}). Similar to ebullition of CH_4, diffusive CH_4 emissions were also highest in summer (16.1 nmol C-CH_4 m^{-2} s^{-1}) and ranged from 0.3 to 64.4 nmol C-CH_4 m^{-2} s^{-1} annually. Diffusive N_2O emissions were also synchronous with ebullition N_2O emissions, with a range of −0.1 to 1.2 nmol m^{-2} s^{-1}, with a seasonal maximum in winter (0.2 nmol N-N_2O m^{-2} s^{-1}), and with negligible fluxes during the remainder of the year.

Ecosystem respiration measured by the eddy-covariance flux tower was highly seasonal but largely decoupled from ebullition and diffusive fluxes, whereas net ecosystem CH_4 exchange was highly synchronous with diffusive and ebullition fluxes (Fig. 5g, h). Daily average ER ranged from approximately 1.0 to 4.0 μmol C-CO_2 m^{-2} s^{-1} with a clear summer peak (3.3 μmol m^{-2} s^{-1}) despite modest seasonality observed via ebullition and diffusion. In contrast, mean daily tower CH_4 fluxes were synchronous with the finer scale measurements, ranging from 0 to 473 nmolC-CH_4 m^{-2} s^{-1}, with a summer maximum of 251 nmol C-CH_4 m^{-2} s^{-1}. However, the spring increase and fall decrease in CH_4 emissions measured by the tower were more gradual than either ebullition or diffusive open-water fluxes. Winter season ER was found to be comparable in magnitude to modeled rates of open-water diffusive CO_2 (Fig. 5a, g) with the exception of spikes in diffusive fluxes during high wind speed events. These data should be comparable during winter because ecosystem production is negligible at this time, and their agreement suggests the empirical wind speed model was a reasonable approach for estimating *k* in the present study.

The relative importance of the different pathways to cumulative GHG emissions depended on the gas considered and season (Table 2). Ebullition was of minor importance for CO_2, accounting for <0.1% of the annual diffusive (915 ± 95 g C-CO_2 m^{-2}) and tower-based (1060 ± 72 g C-CO_2 m^{-2}) flux, whereas diffusive CO_2 flux accounted for a majority (86%) of tower ER. Ebullition and diffusion accounted for approximately 1.3% and 4.1% of flux tower CH_4 emissions (57.5 ± 0.84 g C-CH_4 m^{-2}), respectively, and the majority (>65%) of this was released in summer. Though we did not measure N_2O emissions with eddy covariance, ebullition emissions (27 μg N-N_2O m^{-2}) were negligible (~0.1%) compared with diffusive fluxes (62 400 ± 17 300 μg N-N_2O m^{-2}), and ~84% of annual emissions were released during the winter season.

Table 2. Seasonal and annual cumulative GHG flux from diffusive (mean ± SE), ebullition (downwind (D) vs. upwind (U); median (Q_1–Q_3)) and gap-filled eddy-covariance measurements (±95% CI)

Gas	Measurement	Season				Annual
		Spring	Summer	Fall	Winter	
CO_2 (g C m^{-2})	Diffusive	186	201	211	317	915 ± 95
	Ebullition – D	0.03	0.04	0.04	0.03	0.12 (0.11–0.14)
	Ebullition – U	0.01	0.01	0.03	0.02	0.06 (0.04–0.09)
	Tower – ER	240	341	268	199	1060 ± 72
CH_4 (g C m^{-2})	Diffusive	0.38	1.41	0.35	0.21	2.34 ± 0.41
	Ebullition – D	0.14	0.68	0.22	0	1.03 (0.78–1.36)
	Ebullition – U	0	0.07	0	0	0.07 (0.03–0.09)
	Tower – CH_4	9.7	24.3	18.2	4.6	57.5 ± 0.84
N_2O (μg N m^{-2})	Diffusive	1920	60	7990	52 430	62 400 ± 17 300
	Ebullition – D	7	3	4	13	26 (17–66)

Gas	Measurement	Season				Annual
		Spring	Summer	Fall	Winter	
	Ebullition – U	3	3	5	9	20 (5–102)

- GHG, greenhouse gas.

Radiative forcing effects of ecosystem GHG fluxes

Wetland NEE measured at the flux tower was −325 ± 56 g C-CO_2 m^{-2} yr^{-1} and was offset by CH_4 emissions of 57.5 ± 0.84 g C-CH_4 m^{-2} yr^{-1}, producing a sustained global warming potential (SGWP) of 2.3 ± 0.3 kg CO_2-eq m^{-2} yr^{-1} (Table 3). Tower fluxes, open-water fluxes, and the respective spatial cover fractions (f_{veg}, f_{wat}) were used in a simple mixing model to estimate the parsed vegetation GHG exchange (Figs S5 and S6). The f_{veg} during summer months (Fig. S5) was very close to independent estimates in past work (~0.63; Matthes *et al*., 2014) but showed more variability during winter (Table 3; Fig. S5). Parsed annual vegetation NEE and CH_4 fluxes were larger than open-water exchanges at −1164 ± 298 g C-CO_2 m^{-2} yr^{-1} and 94.8 ± 12.2 g C-CH_4 m^{-2} yr^{-1}, respectively (Table 3). However, the net warming effect of open-water GHG exchange still exceeded that of vegetated zones (Fig. 6). The mixing model indicated that the SGWP of vegetated zones was 1.4 ± 0.3 kg CO_2-eq m^{-2} yr^{-1}, due to high net CO_2 uptake (−4.3 ± 1.1 kg CO_2 m^{-2} yr^{-1}) offsetting the high CH_4 emissions (5.7 ± 0.7 kg CO_2-eq m^{-2} yr^{-1}), whereas open-water fluxes of CO_2, CH_4, and N_2O summed to a SWGP of 3.5 ± 0.3 kg CO_2-eq m^{-2} yr^{-1}.

Table 3. Measured tower and open-water GHG fluxes, mean (±1 SD) annual spatial fractions (f_{veg}, f_{wat}), and model-parsed net GHG fluxes for vegetated zones

Spatial extent	Fraction ($f_{veg/wat}$)	NEE (g C m^{-2} yr^{-1})	CH_4(g C m^{-2} yr^{-1})	N_2O (mg N m^{-2} yr^{-1})	SGWP (kg CO_2-eq m^{-2} yr^{-1})
Tower	Variable	−325 ± 56	57.5 ± 0.8	-	2.3 ± 0.3

Spatial extent	Fraction ($f_{veg/wat}$)	NEE (g C m^{-2} yr^{-1})	CH_4(g C m^{-2} yr^{-1})	N_2O (mg N m^{-2} yr^{-1})	SGWP (kg CO_2-eq m^{-2} yr^{-1})
Water	0.40 ± 0.12	915 ± 96	2.9 ± 0.5	62 ± 17	3.5 ± 0.3
Vegetated	0.57 ± 0.12	−1164 ± 298	94.8 ± 12.3	-	1.4 ± 0.4

- GHG, greenhouse gas; NEE, net ecosystem exchange; SGWP, sustained global warming potential.

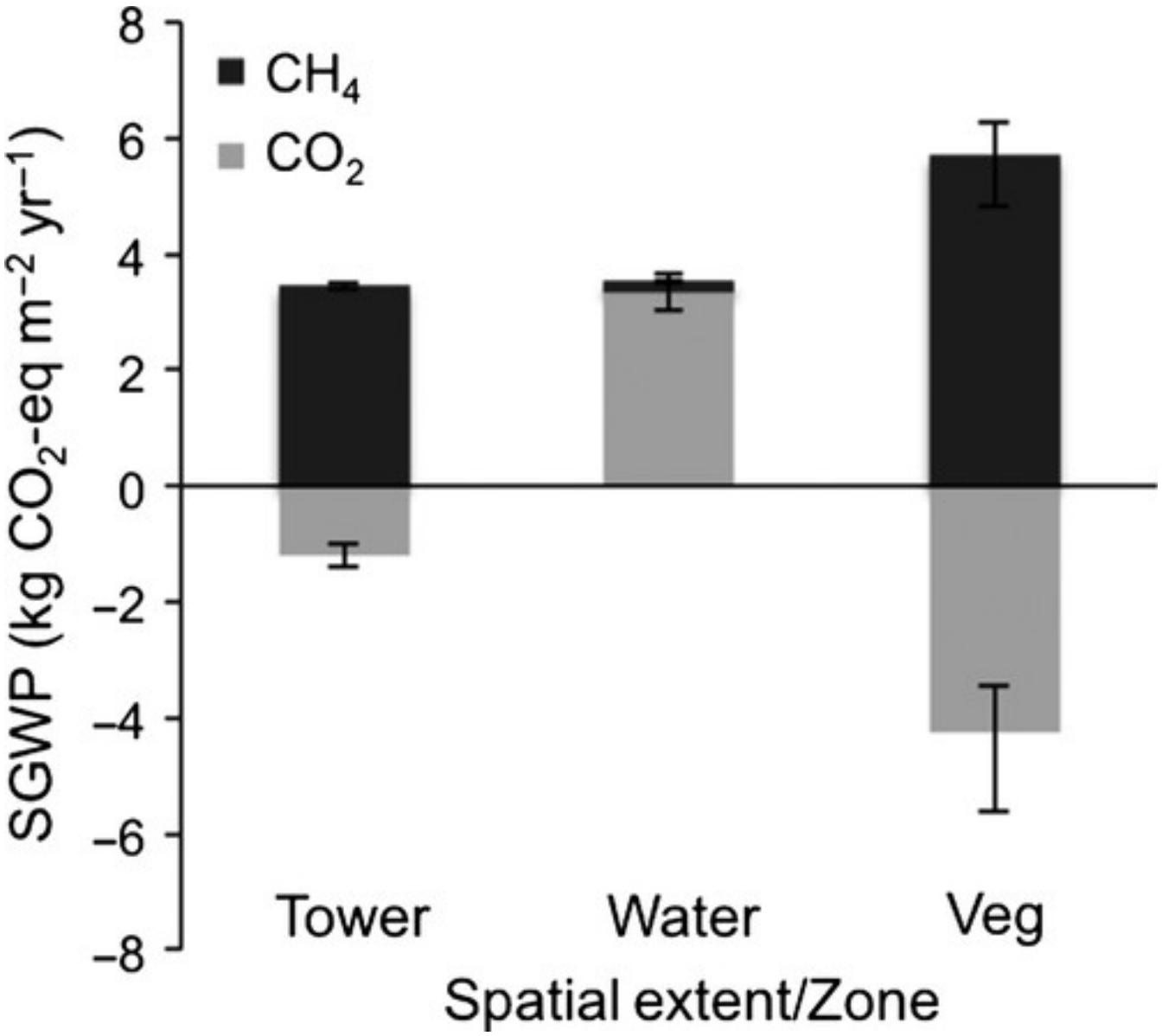

Figure 6

Open in figure viewerPowerPoint

Sustained global warming potential (SGWP) of cumulative annual net CO_2 and CH_4 fluxes measured by the eddy-covariance flux tower (mixed and variable cover type) and separately within open-water and vegetated zones.

Caption

After upscaling to spatial extent of vegetation and open water with in the wetland, total annual GHG fluxes were estimated at −379 ± 153 t C-CO_2 yr^{-1}, 62.3 ± 8.0 t C-CH_4 yr^{-1}, and 66 ± 18 kg N-N_2O yr^{-1}, producing an overall wetland radiative forcing effect of 2.4 ± 0.3 kt CO_2-eq yr^{-1} over a 100-year time horizon (Table 4). The ecosystem switchover time, which refers to the time horizon for the wetland GHG fluxes to change from a net warming effect to a net cooling effect, was estimated from CO_2 uptake to CH_4 emission ratios as contributions from N_2O

were negligible, and GHG fluxes were assumed to be constant over time. Ratios of ~12 and ~6 for vegetation and the entire wetland, respectively, meant that the switchover time for both cover types was >500 years (Table 4). No switchover time occurs for open water as long as both CO_2 and CH_4 fluxes are positive.

Table 4. Wetland zone (vegetated and open-water) spatial extents and associated observed and upscaled estimates of CO_2, CH_4, and GHG fluxes

Spatial extent	Area (m^2)	NEE (t C yr^{-1})	CH_4(t C yr^{-1})	N_2O (kg N y^{-1})	SGWP (kt CO_2-eq yr^{-1})	CO_2:CH_4	Switch (year)
Vegetated	644 672	−750 ± 192	61.1 ± 7.9	–	0.9 ± 0.2	~12	>500
Water	405 520	371 ± 39	1.3 ± 0.2	25 ± 7	1.4 ± 0.1	–	–
Wetland	1 050 192	−379 ± 153	62.3 ± 8.0	66 ± 18	2.4 ± 0.3	~6	>500

- GHG, greenhouse gas; NEE, net ecosystem exchange; SGWP, sustained global warming potential.

Discussion

Spatial patterns in wetland GHG fluxes and radiative forcing

The role of wetland GHG fluxes in global climate change depends on the balance of cooling effects from long-term C sequestration and the warming effects of CH_4 and N_2O emissions (Frolking & Roulet, 2007; Bridgham *et al.*, 2013; Neubauer & Megonigal, 2015). In the present study, high net CH_4 emissions from vegetation dominated the radiative forcing effect of a temperate marsh (5.7 kg CO_2-eq m^{-2} yr^{-1}), with a much smaller contribution from open-water N_2O (0.03 kg CO_2-eq m^{-2} yr^{-1}), and a net cooling effect for vegetation uptake of CO_2(−4.3 kg CO_2 m^{-2} yr^{-1}). These results support emergent marsh wetlands as particularly large CH_4 sources (Whiting & Chanton, 1993; Whalen, 2005; Laanbroek, 2010; Bridgham *et al.*, 2013; Knox *et al.*, 2015) and add to a small but growing body of evidence supporting freshwater

wetlands as dynamic sources of N_2O (Burgin & Groffman, 2012; Moseman-Valtierra, 2012). Our estimates of CO_2 uptake (~1.1 kg C-CO_2 m^{-2} yr^{-1}) were also comparable to others made at nearby wetlands (Miller, 2011; Hatala *et al*., 2012b; Knox *et al*., 2015). However, despite high productivity due to fast-growing, emergent, wetland plants (Bridgham *et al*., 2006), we estimated it would take centuries for CO_2 sequestration to offset the warming effects of CH_4release. There is significant uncertainty in estimates of switchover time based on extrapolations from narrows windows of GHG observations, particularly recently after disturbance or restoration, because assumptions must be made about the persistence of fluxes over time (Neubauer & Megonigal, 2015). Flux observations at Mayberry since reflooding in 2010 suggest interannual variability can be substantial and that ER will gradually decline (Sturtevant *et al*., 2016) which may lead to greater net CO_2 uptake, and reduce ecosystem switchover time. Conversely, GPP may decrease in emergent marshes following accumulation of dead standing litter, which would further postpone switchover (Mitsch *et al*., 2012; Anderson *et al*., 2016). Using multiyear GHG flux observations and modeling of long-term GHG dynamics may greatly improve estimates of switchover time. Such approaches have been applied in the context of hydroelectric reservoir creation (W. Wang, N.T. Roulet, Y. Kim, I.B. Strachan, P. Del Giorgio, Y.T. Prairie & A. Tremblay, in review) and could be applied similarly to wetlands. It is clear that the expected longevity of restored wetland ecosystems and the persistence of their GHG fluxes are therefore key for understanding the overall climate forcing effects. Restored wetlands are often rapidly colonized by *Typha* spp. as was the case in the present study, and these rapid colonizer plants support extremely high rates of gas exchange with the sediment (Laanbroek, 2010; Moreno-Mateos *et al*., 2012). Shifts in vegetation composition following restoration could therefore result in changes in CH_4 flux and GHG forcing of the wetland. We also emphasize that the value of wetland restoration cannot be determined by the sole metric of GHG radiative forcing. In the present study, important ecological cobenefits are at stake including habitat restoration, peat soil rebuilding, and levee stabilization (Miller, 2011; Moreno-Mateos *et al*., 2012; Hatala *et al*., 2012b; Knox *et al*., 2015; Anderson *et al*., 2016).

Wetland restoration can optimize ecological and biogeochemical functions by managing hydrologic flow and the distribution of vegetation (Moreno-Mateos *et al*., 2012). We investigated spatial patterning of open water and vegetation as drivers of spatial variability in GHG exchange. We found very high net CO_2 uptake concentrated in zones of emergent vegetation was strongly offset by high CO_2 emissions in open water. After estimating the SGWP for the two zones separately, we found that open water emitted more GHG (3.5 kg CO_2-eq m^{-2} yr^{-1}) than vegetated areas (1.4 kg CO_2-eq m^{-2} yr^{-1}), suggesting that a greater extent of emergent vegetation in some restored wetlands could be favorable from a GHG perspective. Similarly, Stefanik & Mitsch

(2014) concluded vegetation was a favorable cover type in created wetlands in Ohio due to no significant difference in CH_4 efflux between open water and emergent vegetation. Our result is more surprising given the much higher CH_4 emissions from vegetation, but the high CO_2 emissions may be particular to deep peat wetland soils of the California Delta (Drexler *et al*., 2009a,b). The organic C content of wetland soil can regulate the net effect of vegetation on C gas exchange (Laanbroek, 2010), and fermentation and decomposition of deep peat are consistent with a persistent, large, and spatially dispersed source of CO_2. It is also possible that the legacy of drainage at the site continues to support elevated rates of CO_2 production from underlying peat that may slow down as the site ages (Moreno-Mateos *et al*., 2012). Furthermore, biogeochemical function in these two wetland zones is connected as C inputs in vegetated zones likely fuel some of the GHG ultimately emitted via open-water pathways. Other interactions between these zones include the influence of vegetation canopies on whole-wetland temperature, light availability, and wind speed. It is clear, however, that the mix of vegetation and open water for optimal radiative forcing in restored wetlands will depend on both the current rate of CO_2 and CH_4 exchange above vegetation and the background rate of C gas production from flooded soil, which likely influenced by depth and organic content.

Decoupling of ebullition and CH_4 content

Spatial patterning of vegetation and open water also affects the dominant pathways for wetland GHG emission (Bridgham *et al*., 2013). We used a highly replicated design to estimate open-water ebullition fluxes, a pathway that dominates CH_4 release in deeper aquatic environments (Wik *et al*., 2013) and can bypass oxidation processes even in shallower wetlands (King, 1990). We found low rates of CH_4 release via this pathway (~1 g C-CH_4 m^{-2} yr^{-1}) relative to fluxes from zones of emergent vegetation (94.8 g C-CH_4 m^{-2} yr^{-1}). Ebullition fluxes were attenuated by low CH_4 content during most of the year. Had CH_4 content been fixed at the summer fraction (30–50%), year-round ebullition CH_4 emissions would have been comparable to emission rates via diffusion (~5% of total emissions).

The observed decoupling of ebullition fluxes and CH_4 content is surprising given that previous work has shown CH_4 content to correlate with ebullition rates (Chanton *et al*., 1989) and current understanding attributes ebullition bubble growth to excess partial pressure of CH_4 in wetland soils (Scandella *et al*., 2011; Green, 2013). Back-diffusion from the ebullition chamber headspace into the water column could produce a randomly distributed underestimation of CH_4 content on a weekly basis (Varadharajan *et al*., 2010), and could exhibit seasonality with lower winter temperatures increasing gas solubility. However, we do not think back-diffusion alone can explain the consistent seasonal variation in content over four orders of magnitude.

Instead, we hypothesize that the thick layers of sapric peat at the restored wetland facilitated bubble formation at depth, and CH_4 was lost during bubble migration to the wetland surface during seasons of low dissolved CH_4 (Scandella *et al*., 2011), related to both temperature and changes in the balance of CH_4 production and consumption in general. The CH_4 partial pressure in surficial peat layers is likely to vary seasonally across several orders of magnitude, as was found clearly for surface dissolved CH_4. We therefore propose that bubbles retain high CH_4 content during migration and release in the summer when high pore-water CH_4 is maintained throughout the peat profile. In contrast, when surficial CH_4 concentrations are much lower in winter, dissolution and oxidation of CH_4 act to strip the bubble of CH_4 before ebullitive release. Some studies have found patterns in bubble CH_4 content associated with spatial variability in sediment C content, vegetation type, and water depth (Martinez & Anderson, 2013; Wik *et al*., 2013; Crawford *et al*., 2014; Hamilton *et al*., 2014). To the best of our knowledge, this study is the first to show seasonal decoupling of ebullition rate and CH_4content that acted to attenuate annual CH_4 emissions via this pathway. We encourage further work to consider how ebullition gas content may be modulated during migration from deep peat or sediment layers.

Asynchronous seasonality in wetland CH_4 and N_2O

Simultaneous measurement of CO_2, CH_4, and N_2O fluxes can also provide new insights into ecosystem function, especially given the differences in the biogeochemical conditions that facilitate production and consumption. In the present study, the observation of strong seasonal asynchronicity between open-water CH_4 and N_2O inventories (Fig. 4) highlights the limitations of simple empirical functions, such as temperature relationships, for interpreting or predicting ecosystem GHG fluxes (Davidson & Janssens, 2006). Enhanced N_2O efflux during the cool winter season plainly contradicts an Arrhenius prediction that microbial activity and associated GHG production will scale exponentially with temperature. Rather, both the observed threshold effect and asynchronous dynamics in wetland N_2O and CH_4concentrations are consistent with a redox mechanism (Helton *et al*., 2015). Persistent or fluctuating aerobic conditions favor N_2O production and CH_4 consumption, whereas persistent anaerobic conditions favor the reverse (Firestone & Davidson, 1989; Hanson & Hanson, 1996). Changing the relative predominance of aerobic and anaerobic zones in wetland soils will therefore strongly favor either N_2O or CH_4 efflux (McNicol & Silver, 2014). High summer temperatures likely increased biological O_2 demand, favoring the production of reduced gases (CH_4 and N_2). In contrast, lower winter temperatures and ecosystem C inputs likely favored oxidized gas species (CO_2, N_2O). Our data support the kinetic effects of temperature as an intrinsic control of microbial function that are

superimposed on, and feedback to, extrinsic controls such as local redox environment of microbial communities (Von Fischer & Hedin, 2007; Davidson & Janssens, 2006).

We used a two-scale approach to quantify annual wetland GHG fluxes and their associated radiative forcing effects and then linked patterns to seasonality, vegetation structure, and transport pathway. The wetland was a net sink for CO_2 despite high background rates of CO_2emission measured in the open-water zones. In contrast, the wetland was strong source of CH_4 with the vast majority emitted from vegetated zones. Although ebullition bubble fluxes were substantial, seasonally low CH_4 content reduced the importance of this transport pathway for CH_4 emission at the annual timescale. Diffusive CH_4 fluxes were of comparable magnitude to those from ebullition, and together represented <10% of whole-ecosystem emissions. The overall SGWP of fluxes highlight the disproportionate role of emergent vegetation on both CO_2 uptake and CH_4 emission in freshwater wetlands. Although unimportant to wetland radiative forcing, N_2O fluxes and their seasonal asynchronicity with CH_4 emissions were consistent with wetland redox oscillations as a unifying driver of wetland GHG dynamics. We encourage further work to couple biophysical drivers of plant and microbial function to GHG production, using a framework of redox thermodynamics as the proximate control.

Acknowledgements

We thank Jackson Chin, Heather Dang, Ryan Salladay, and Laura Southworth for assistance with field data collection. We are also grateful for advice from Charuleka Varadharajan on adapting ebullition flux chamber designs, and to anonymous reviewers for useful comments on earlier versions of this manuscript. This research was supported by the Delta Science Program grant (#2053) and an NSF Doctoral Dissertation Improvement Grant (DEB-1405715). This research was also supported by the USDA National Institute of Food and Agriculture McIntire Stennis project CA-B-ECO-7673-MS 450 to W. Silver. GM was also supported as a Lawrence Graduate Scholar at Lawrence Livermore National Laboratory and as a Research Fellow of the University of California Carbon Neutrality Initiative.

Author contribution

GM and WS designed the study, GM conducted the chamber sampling while SK, CS, and DD oversaw and processed eddy-covariance flux observations. ID contracted the remote sensing imagery and conducted the spatial classification (supported by the Delta Science Program grant #R/SF-52 and Geospatial Innovation Facility at UC Berkeley, gif.berkeley.edu), CS developed the R code for spatial fraction estimation, and GM authored the manuscript.